MOX-Report No. 43/2016

A multiscale modeling approach to transport of nano-constructs in biological tissues

Ambrosi, D.; Ciarletta, P.; De Falco, C.; Taffetani, M.; Zunino, P.

MOX, Dipartimento di Matematica
Politecnico di Milano, Via Bonardi 9 - 20133 Milano (Italy)

mox-dmat@polimi.it http://mox.polimi.it

Chapter 1
A multiscale modeling approach to transport of nano-constructs in biological tissues

Davide Ambrosi and Pasquale Ciarletta and Carlo de Falco and Matteo Taffetani and Paolo Zunino

Abstract Nanomedicine is the emerging medical research branch which employs nanotechnological devices to improve clinical diagnosis and to design more effective therapeutic methodologies. In particular, functionalized nanoparticles have proved their clinical usefulness for cancer therapy, either as vectors for targeted drug delivery or for hyperthermia treatment. The effectiveness of such novel therapeutic strategies in nanomedicine exploits the capability of the nanoparticles to penetrate into the living tissue through the vascular network and to reach the targeted site. Accordingly, their success is tightly related to the control of the the multi-physics and multi-scale phenomena governing the diffusion and transport properties of the nanoparticles, together with the geometrical and chemo-mechanical factors regulating the nanoparticles-tissue interactions. Indeed, the therapeutic effectiveness of earlier approaches was hindered by a limited ability in penetrating within the tumor tissue essentially due to microfluidic effects. Mathematical modeling is often employed in nanomedicine to analyze *in silico* the key biophysical mechanisms acting at different scales of investigations, providing useful guidelines to foresee and possibily optimize novel experimental techniques. Since these phenomena involve different characteristic time- and length-scales, a multi-scale modeling approach is mandatory. In this work we outline how a multi-scale analysis starts at the smallest scale, and its results are injected in large-scale models. At the microscale, the transport of nanoparticles is modeled either by the stochastic Langevin equation or by its continuous limit; in both cases short distance interaction forces between particles are considered, such as Coulomb and van der Waals interactions, and small disturbances of the fluid velocity field induced by the presence of nanoparticles are assumed. At the macroscopic scale, the living tissue is typically modeled as a homogeneous (homogenized) porous material of varying permeability, where the fluid flow is modeled by Darcy's equation and nanoparticle transport is

Davide Ambrosi
MOX, Dipartimento di Matematica Politecnico di Milano, e-mail: davide.ambrosi@polimi.it

Pasquale Ciarletta
MOX, Dipartimento di Matematica Politecnico di Milano, e-mail: pasquale.ciarletta@polimi.it

Carlo de Falco
MOX, Dipartimento di Matematica Politecnico di Milano, e-mail: carlo.defalco@polimi.it

Matteo Taffetani
Mathematical Institute University of Oxford, e-mail: matteo.taffetani@maths.ox.ac.uk

Paolo Zunino
MOX, Dipartimento di Matematica Politecnico di Milano, e-mail: paolo.zunino@polimi.it

described by a continuum Diffusion-Reaction-Advection equation. One of the most significant features of the model is the ability to incorporate information on the microvascular network based on physiological data. The exploitation of the large aspect ratio between the diameter of a capillary and the intercapillary distance makes it possible to adopt an advanced computational scheme as the *embedded multiscale method*: with this approach the capillaries are represented as one-dimensional (1D) channels embedded and exchanging mass in a porous medium. Special mathematical operators are used to model the interaction of capillaries with the surrounding tissue. In this general context, we illustrate a *bottom-up* approach to study the transport and the diffusion of nanoparticles in living materials. We determine the permeability as well as the lumped parameters appearing in the nanoparticle transport equation at the tissue level by means of simulations at the microscale, while the macroscale tissue deposition rate is derived from the results of microscale simulations by means of a suitable upscaling technique.

1.1 Biophysics of cancer

Transport phenomena play a fundamental role in the development of cancer. At different phases of cancer disease, tumors use mass transport to interact with the surrounding environment [32]; the propagation of growth signals or the invasion of the surrounding tissue by initiation of angiogenesis are essentially regulated by transport phenomena. Transport phenomena are also at the basis of the pharmacological treatment of cancer. The vascular network is a natural therapeutic option to target vascularized tumors. Nevertheless, the success of anticancer therapies in treating cancer cells *in vivo* is limited by their inability to reach their target in adequate quantities [33]. An agent that is delivered intravenously reaches cancer cells exploiting the vascular flow, then it crosses the vessel wall and diffuses through the tissue interstitium. Each of these steps can be seen as a barrier to delivery. In addition, even delivered molecules may bind to constituents of the extracellular matrix and be metabolised by cells.

The characteristic traits of cancer can be seen as the emergent behavior of a cascade of phenomena that propagate from the molecular scale, through the cell and the tissue microenvironment, up to the systemic level. Transport phenomena in the capillary network (the *microenvironment* or *microscale*) play a key role in this sequence of effects. In particular, the alterations of the capillary phenotype of a tumor significantly affect the drug delivery process [9]: blood vessels in tumors are leakier and more tortuous than the normal microvasculature and the pressure generated by the proliferating cells reduces tumor blood and lymphatic flow. These alterations lead to an impaired blood supply and abnormal tumor microenvironment, characterized by hypoxia and elevated interstitial fluid pressure. The reduced pressure gap across the vessel walls is sometimes even reversed in sign and greatly reduces the ability to deliver drugs.

The mathematical modelling of interstitial flow can be an important support to tackle these issues. The objective of this work is to illustrate a multiscale mathematical model to investigate the diffusion and transport properties of nanoparticles after nanofluidic injection into a living tissue. Our multiscale approach is based on two coupled models. The macroscopic model considers the tissue as a porous medium, and accounts for convection, diffusion and absorption of the particles, by means of a continuous spatial concentration. The microscopic model studies the motion of the particles in the extra-cellular space and their interaction with the targeted cell surface. We follow the definition of characteristic scales proposed in [56]:

- (i) The tissue scale (cm-tens of s), where the structured heterogeneities within the living material can be separately recognized;
- (ii) The extravascular space (mm-s), where the matter trasfers from blood in the capillary network to the extracellular matter and the cells;

- (iii) The cellular level (μm-ms), in which nanoparticles/nanovectors diffuse and are advected by the flow or up-taken by the cells, behaving like a suspension within a fluid domain;
- (iv) The sub-cellular level (up to hundreds of nm-μs), where the biochemical interactions, such as the particles uptaking or cells regulation, become the dominant processes.

The models labelled as *macroscale* span the scales between (i) and (ii), while the *microscale* typically involves phenomena of (iii) and (iv).

1.1.1 An overview of transport phenomena in tumors

Several mathematical models have been proposed in recent years to describe transport phenomena in tumor tissues, and different types of particles have been used in cancer treatment. In most cases, the tumor is assumed to be spherical, in analogy with the multi-cellular tumor spheroid model, an assumption that allows to exploit the radial symmetry; in general the significant parameters are considered constant and derived experimentally.

Banerjee *et al.* [5] described the penetration of monoclonal antibodies in a tumor nodule surrounded by healthy tissue. The nodule is assumed to be spherical and embedded in a tissue described by a macroscale model: the concentration of free antibodies in the external extracellular space is determined by the interaction between diffusion, uptake from blood and efflux to lymphatics. The distance between blood and lymphatic microvessels is assumed to be small in comparison with the tumor nodule and then uptake and efflux can be described by uniform rate constants. Exploiting the radial symmetry, the concentration of antibodies A_b in the healthy tissue

$$\frac{\partial A_b}{\partial t} = D_e \frac{1}{r^2}\frac{\partial}{\partial r}\left(r^2 \frac{\partial A_b}{\partial r}\right) + \kappa A_{b,p} - \Lambda A_b, \tag{1.1}$$

where $A_{b,p}$ is the concentration of antibodies in the blood, r is the radial coordinate, t is time, D_e is the diffusion coefficient in the healthy tissue, κ is the constant rate of transcapillary exchange, Λ is the constant rate of lymphatic flux from normal interstitium.
In cancer in a pre-vascular stage the presence of lymphatic and blood vessels is neglected and can be described as in van Osdol [43] and Graff and Wittrup [31]. The concentration of free antibodies is coupled to the concentration of free antigens and to the concentration of the antigen-antibody complex B by the reaction terms,

$$\frac{\partial A_b}{\partial t} = D \frac{1}{r^2}\frac{\partial}{\partial r}\left(r^2 \frac{\partial A_b}{\partial r}\right) - k_f A_b A_g + k_r B, \tag{1.2a}$$

$$\frac{\partial A_g}{\partial t} = n(-k_f A_b A_g + k_r B), \tag{1.2b}$$

$$\frac{\partial B}{\partial t} = k_f A_b A_g - k_f B, \tag{1.2c}$$

$$A_g + nB = A_{g,0}, \tag{1.2d}$$

where k_f and k_r are constants that describe the association and dissociation rates between antibodies and antigens, $n = 2$ is the binding valence of antibodies, $A_{g,0}$ is the total concentration of antibodies. The authors considered symmetric Dirichlet boundary conditions and a condition of interface between the tumor and the normal tissues. All constants in the model were determined experimentally; among all parameters, the

diffusion coefficient is very difficult to measure, thus explaining the large variability in the values that can be found in the literature. Numerical simulations show that the values chosen for the diffusion coefficient and the density of the binding sites in the tumor (in this case the antigens) play a fundamental role in the diffusion of the particles.

Graff and Wittrup [31] used a very similar model to describe the diffusion of antibodies in tumor spheroids. Their results are compared with those experimentally obtained in tumor spheroids and no healthy tissue is considered. The study focuses on the optimization of the affinity antibody/antigen. In previous simulations [43] it had been shown that the high affinity antibody/antigen was responsible for the formation of a *binding site barrier*: the front of free antibodies advances inside the spheroid until their concentration in plasma falls below a certain level. If the front stops when antibodies have not yet reached the center of the spheroid, they create a "barrier". The study shows that antibodies with lower affinity have a greater penetration ability, but their therapeutic efficacy decreases. Also in this model the association and dissociation rates are assumed to be constant and the convection within the tumor is neglected.

Ward *et al.* [60] and Norris *et al.* [41] propose a refined model for the diffusion of chemotherapic drugs in tumor spheroids and used it to compare the effectiveness of various techniques of drug release. The numerical analysis applies to a system of four one-dimensional equations in radial coordinates where different fields are considered: the density of living cells, the concentration of nutrients, the concentration of drug and the convective flow of the cells in the spheroid. The reaction terms account for mitosis and apoptosis rates of the cells: the former according to a generalized Michaelis-Menten kinetics, while the rate of cell death depends on the concentration of drug.

The models presented above are designed for the diffusion and transport of macromolecules and antibodies, and they can not be directly applied to the diffusion and transport of nanoparticles: nanoscale objects are subject to strong interaction with the cellular surface, that may cause further absorption with respect to the simply due the molecular degradation. Moreover the diffusivity of the nanoparticles is smaller than for macromolecules, since the Brownian motion, due to collisions of the particles with the molecules of the fluid, is inversely proportional to the particles size. Goodman *et al.* [30] analyzed the diffusion of nanoparticles for size between 20 and 200 nm and developed a mathematical model which takes into account the inhomogeneities inside the tumor spheroids. They assume that the porosity ε depends on the radial coordinate and such a generalization allows the application of the model to spheroids treated with collagenase. In fact, it is experimentally known that the treatment of spheroids with ECM-degrading enzymes, such as collagenase and ialuronidase, the increases of the pore volume (as shown in Figure 1.1) and therefore facilitates the diffusion of the particles.

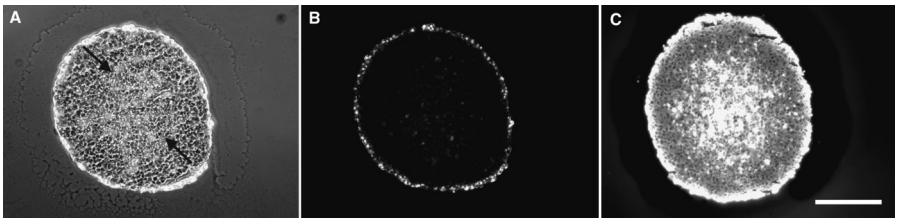

Fig. 1.1 Sections of a spheroid exposed to 40 nm fluorescent nanoparticles. (A) Section shown as a phase contrast; arrows indicate the approximate boundary of the necrotic core. (B) Section shown as a fluorescent image. (C) Fluorescent image of a spheroid coincubated with 0.076 mg/mL collagenase and nanoparticles. Scale bar is 200 μm. [30]

The model by Goodman *et al.* describes the evolution of the molar concentration C of free particles, the concentration of bound particles C_b, the concentration of available binding sites on the cell surface C_{bs}, the concentration of internalized particles C_i. The corresponding balance equations are

$$\frac{\partial C}{\partial t} = \frac{1}{r^2}\frac{\partial}{\partial r}\left[D\varepsilon r^2 \frac{\partial}{\partial r}\left(\frac{C}{\varepsilon}\right)\right] - k_a C_{bs}\frac{C}{\varepsilon} + k_d C_b, \tag{1.3a}$$

$$\frac{\partial C_b}{\partial t} = k_a C_{bs}\frac{C}{\varepsilon} - k_d C_b - k_i C_b, \tag{1.3b}$$

$$\frac{\partial C_{bs}}{\partial t} = -k_a C_{bs}\frac{C}{\varepsilon} + k_d C_b + k_i C_b, \tag{1.3c}$$

$$\frac{\partial C_i}{\partial t} = k_i C_b, \tag{1.3d}$$

where k_a is the rate of association, k_d the rate of dissociation, k_i the rate of internalization. We point out that the porosity of the material ε is not an asymptotically small parameter in this setting and recall that it may depend on the radial coordinate, namely $\varepsilon = \varepsilon(r)$. The initial and boundary conditions are given by

$$\begin{aligned} C(0,r) = C_b(0,r) = C_i(0,r) &= 0, \qquad 0 \le r < R, \\ C_{bs}(0,r) &= C_{bs,0}, \qquad 0 \le r < R, \\ C(t,R) &= C_0\varepsilon(R), \qquad t > 0, \\ \frac{\partial}{\partial r}\left(\frac{C}{\varepsilon}\right)(t,0) &= 0, \qquad t > 0, \end{aligned} \tag{1.4}$$

where R is the radius of the spheroid, C_0 is the concentration of particles outside the spheroid and $C_{bs,0}$ is the initial concentration of the binding sites inside the spheroid.

The model is formally analogous to the one by [31], while it considers the particles internalization. The article highlights the difficulty in finding an expression for the diffusion coefficient in tumor tissue that should sinthetically represent various factors (such as the arrangement of the cells and the composition of the extracellular matrix). A possible expression for the diffusion coefficient in porous media is given by [30]

$$D = D_0 \frac{L(\lambda)}{F\tau(\varepsilon)}, \tag{1.5}$$

where

$$D_0 = \frac{K_B T}{6\pi\eta r_p}, \qquad \text{and} \qquad \lambda = \frac{r_p}{r_{pore}}. \tag{1.6}$$

Here D_0 is the diffusion coefficient in an unbounded liquid medium, r_p is the particle radius, r_{pore} is the effective pore size, η is the fluid viscosity, K_B is the Boltzmann constant, T is the absolute temperature, $L(\lambda)$ is the factor responsible for hydrodynamic and steric reduction of the diffusion coefficient in the pore, $\tau(\varepsilon)$ is the tortuosity and $F > 1$ is a shape factor that accounts for the hindrance in the pores. While this model considers non-specific interactions, it shows that the diameter of the nanoparticles is a fundamental parameter for the diffusion of the drugs and introduces the space-dependent porosity ε as an approach for modeling the heterogeneity of the tissue.

The model proposed by Goodman has been seminal in the field. Different expressions for the diffusion coefficient have been later proposed by Florence [25] and Gao *et al.* [27]. The former author proposes various expressions for the diffusion coefficient, taking into account the obstacles present in the extracellular matrix.

The second one compares the model-simulated results on the diffusion of nanoparticles with experimental results obtained in the case of three different types of nanoparticles with positive, negative and neutral charges, respectively.

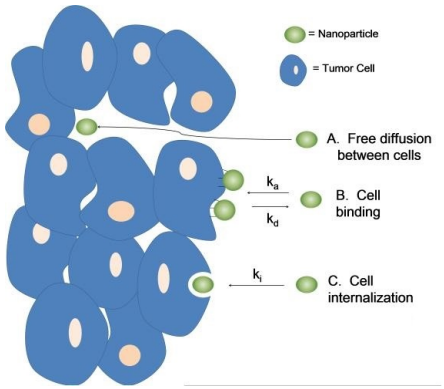

Fig. 1.2 Transport mechanisms governing nanoparticles penetration through solid tumors. Nanoparticles are transported through tumors by (A) free diffusion in extracellular space, and can be inhibited by (B) cell binding and/or by (C) cell internalization. The structure of nanoparticles can be tuned to alter their interactions with cells and the tumor bed, thus optimizing their transport through solid tumors. [59]

Waite and Roth [59] applied a model similar to the one by Goodman to a particular kind of nanoparticles (dendrimers PAPAM) simulating the effect of the change in the number of targeting ligands (RGD peptides) on their surface. The affinity of these ligands with a malignant glioma cells had been demonstrated experimentally. This type of particles is positively charged and exerts electrostatic interactions with the cell membrane. The previous models are expanded to include two possible modes for the formation of bonds between nanoparticles and cells: through receptor-mediated interactions (between RGD targeting peptides and cell-surface integrin proteins) or non-specific ones (through electrostatic interactions). The differential system (1.3) is supplemented by the equations for the concentration of particles linked to specific binding sites and for the concentration of available specific binding sites. Graff and Wittrup have shown that low affinity antibodies have a more homogeneous distribution through solid tumours; in this paper a similar behavior is observed in the case of tumor-targeted nanoscale materials. Unlike in Goodman analysis, the porosity is assumed to be constant through the spheroid, as well as the diffusion coefficient and the association and dissociation rates, which are estimated through the comparison with experimental data.

A similar model was obtained in Ying *et al.* [61] for the transport of drugs through vesicles, which have been studied along several years for their ability to deliver drugs. In particular, various methods were evaluated for the calculation of the coefficient of association between receptors and specific ligands, considering also the possibility to use different types of ligands on a single vesicle. In this work, no formation of non-specific binding is considered.

At the sub-cellular level, the theory proposed by Decuzzi and Ferrari [19, 20] studies the specific interactions between cells and particles to assess the relation between the dynamics of absorption and the shape of the particles. The absorption rate of the particles is then a function of the binding energy, the density and mobility of receptors on the cell membrane and the shape of the particles.

Chou *et al.* [14] adopted a different point of view and constructed a small-scale model to study the evolution of macromolecule carriers in localized tumor tissues. While the articles presented above considered

spheroids tumor or tumors in pre-vascular phase, in this case a convective flux of the interstitial fluid is taken into account.

Su *et al.* [55] studied a multiscale model for the transport and deposition of magnetite nanoparticles during the injection of nanofluids into tumor tissues. They track the trajectory of a particle in the extracellular matrix through the study of its dynamics and the interactions between the nanoparticle and a cell; this study allows to obtain the rate of particles deposition on a single cell, from which the volumetric absorption coefficient in the tissue can be computed and then used in a macroscale model.

1.2 A micro-scale approach to transport of nano-constructs

1.2.1 Microscopic model

In this section we restrict our analysis to motion of nanoparticles in the extracellular space, around either a single cell or in a pore, with the aim of determining the single cell efficiency η_s as a function of the relevant biophysical phenomena. The hydrodynamic interactions between the particles can be neglected since the nanofluid is dilute and the nanoparticles behave as point-like, chemically inert, solid spheres.

Due to the small length-scales under considerations, the flow is characterized by a very small Reynolds number, it is laminar and obeys the Stokes equations

$$\begin{cases} \nabla p = \eta \Delta \mathbf{v}_f, \\ \nabla \cdot \mathbf{v}_f = 0, \end{cases} \tag{1.7}$$

where p is the pressure and $\mathbf{v}_f$ is the fluid velocity. In the following, we solve these equations for given pressure drop at the boundary, no slip conditions on the cell surface and boundary conditions dictated by the symmetry of the problem elsewhere.

The nanoparticles around a cell are subject to the drift of the flowing liquid, while their motion is affected by Brownian motion and other forces (see Sect. 1.2.1.2). Accordingly, the distribution of the nanoparticles can be modeled through either a discrete stochastic approach, which calculates the trajectory of the particles, or through its continuous limit, which studies the evolution of nanoparticle density in time and space.

Using the discrete viewpoint, the trajectory of a nanoparticle is described by the stochastic Langevin equation:

$$d\mathbf{r}_j = \left(\frac{D}{K_B T} \mathbf{F}^e + \mathbf{v} \right) \Delta t + (\Delta \mathbf{r})_j^B, \tag{1.8}$$

where $d\mathbf{r}_j$ is the displacement vector of the jth particle, D is the particle diffusivity tensor, $\mathbf{F}^e$ represents the sum of all the forces acting on the particle, $\mathbf{v}$ is the particle velocity, Δt is the time step and $(\Delta \mathbf{r})_j^B$ is the random Brownian displacement due to collisions between the particles and the fluid molecules surrounding them. Moreover K_B is the Boltzmann constant and T is the absolute temperature. Since nano-sized-particles have a small relaxation time, we can neglect inertia and assume that the particles relax to the fluid velocity almost instantaneously. Thus, the particle velocity $\mathbf{v}$ coincides with the fluid velocity.

Conversely, using a continuous viewpoint, the evolution of the nanoparticles concentration c can be described by the following advection-diffusion equation

$$\frac{\partial c}{\partial t} - \nabla \cdot \left(D\nabla c - \mathbf{v}c - \frac{1}{K_B T} D\mathbf{F}^e c \right) = 0, \tag{1.9}$$

where D is a diffusivity tensor. The next section is devoted to the identification of the major factors influencing the microscopic motion of the nanoparticles in the extracellular space: the hydrodynamic interactions and the forces acting on the nanoparticles.

1.2.1.1 Hydrodynamic retardations

The diffusivity tensor D and the nanoparticle velocity $\mathbf{v}$ appear in both equations (1.8) and (1.9). Since inertia is negligible, the nanoparticle velocity $\mathbf{v}$ can be assumed to coincide with the fluid velocity. Far from the cell surface, the perturbation of the nanoparticle on the flowfield can be neglected and the velocity of the fluid obeys to Stokes equations (1.7) without any feedback. Similarly, the nanoparticle diffusivity can be assumed to be isotropic according to Stokes-Einstein relation far away from the cell. Conversely, near the cell the hydrodynamic interactions between the particles and the cell surface significantly affect the motion of the fluid, thus influencing the induced particle velocity and diffusivity [29, 28]. Since the nanoparticles are much smaller than a cell and the perturbation to the fluid flow is significant only near the cell surface, this one can be approximated as a plane wall and the following relations can be introduced [21]

$$\begin{aligned} v_{\parallel} &= f_3(\delta) v_{f,\parallel} \quad , \qquad v_{\perp} = f_1(\delta) f_2(\delta) v_{f,\perp}, \\ D_{\parallel} &= f_4(\delta) D_0 \quad , \qquad D_{\perp} = f_1(\delta) D_0, \end{aligned} \tag{1.10}$$

where the subscripts $\parallel$ and $\perp$ indicate the components in the direction parallel and perpendicular to the surface, respectively. The scalar functions f_i, $i = 1, \ldots, 4$ depend on the normalized distance δ, defined as the ratio between the distance H of the particle center from the cell surface and the particle radius r_p. Their values can be fixed by estimating the hydrodynamic forces and torques acting on a particle near the surface and exploiting the equilibrium equations. In our simulations, we used the values obtained computing these functions by numerically solving four test cases and validating our results with the approximated expressions presented in [55].

1.2.1.2 Driving forces

When a particle moves immersed in the fluid filling the extracellular space, several forces should be considered: drag, Basset force, Magnus force, Saffman force and buoyancy force. Nevertheless, all the mentioned forces can be neglected in our study due to the small size of the particles considered. In our microscopic model, we take into account only two type of interactions between the nanoparticles and the cell:

$$\mathbf{F} = \mathbf{F}_{lift} + \mathbf{F}_{DLVO}, \tag{1.11}$$

where $\mathbf{F}_{DLVO}$ represents the sum of Derjaguin, Landau, Verwey, and Overbeek (DLVO) forces and $\mathbf{F}_{lift}$ the lift force. All of these contributions act normally to the cell surface and are significant when the particle is close to the cell surface.

The DLVO theory quantitatively explains the aggregation of aqueous dispersions and is based on the combined effect of two forces: the van der Waals force and the electrostatic double layer force. The latter arises only between charged bodies through an electrolyte solution and it will be neglected in the following

since we deal with non charged nanoparticles. The van der Waals intermolecular force due to interactions between the dipoles constituting the bodies, which is given by:

$$\mathbf{F}_{DLVO} = -\frac{\partial U_{vdW}}{\partial h}, \tag{1.12}$$

where h is the distance between the two surfaces and U_{vdW} is the van der Waals interaction energy. An approximate expression for U_{vdW} between a sphere of radius r_p and a plane wall is given by [35]

$$U_{vdW} = -\frac{A_H}{6}\left(\frac{r_p}{h} + \frac{r_p}{2r_p+h} + \ln\frac{h}{2r_p+h}\right), \tag{1.13}$$

where A_H is the Hamaker constant.

The lift force acts on a nanoparticle which moves in a fluid flowing close to a surface: in this condition, the gradient of velocity tends to move the particle in the direction normal to the streamlines of the fluid flow. The lift force acting on a neutrally buoyant particle in a fluid having a linear shear flow profile near a wall is given by [13]

$$\mathbf{F}_{lift} = r_p \eta V Re I \mathbf{i}_{\perp}, \tag{1.14}$$

where I is such that

$$\begin{aligned} I = &\left(1.7631 + 0.3561\zeta - 1.1837\zeta^2 + 0.845163\zeta^3\right) + \\ &- \left(3.24139\zeta^{-1} + 2.6760 + 0.8248\zeta - 0.4616\zeta^2\right)\Lambda_G + \\ &+ \left(1.8081 + 0.879585\zeta - 1.9009\zeta^2 + 0.98149\zeta^3\right)\Lambda_G^2, \end{aligned} \tag{1.15}$$

with

$$\zeta = \frac{r_p}{H} \quad , \quad \Lambda_G = \frac{G r_p}{V}. \tag{1.16}$$

In equations (1.14)-(1.16) V is a characteristic velocity, Re is the Reynolds number calculated using the particle radius, H is the distance of the particle center from the cell surface and G is the velocity gradient of the linear shear flow field in the direction normal to the surface.

1.2.1.3 Microscopic geometry

In the study of particles deposition onto solid surfaces, Happel's sphere-in-cell model has been extensively applied as a representation of the unit cell constituting the porous medium [48, 58, 40]. In this model the medium is represented as an assembly of identical spherical cells of radius r_c, each one surrounded by a shell of fluid (Fig. 1.3); the outer boundary is a concentric sphere of radius b, where b is chosen so that the overall porosity of the medium is preserved for the single cell, that is

$$b = r_c(1-\varepsilon)^{-\frac{1}{3}}, \tag{1.17}$$

as shown in Fig. 1.3(left). The axial symmetry of the problem allows an analytical solution of Stokes equation (1.7). In particular, the components of the fluid velocity can be obtained in spherical coordinates [21] as a function of the uniform fluid velocity U_∞ far away from the cell. Nonetheless, this model is not well

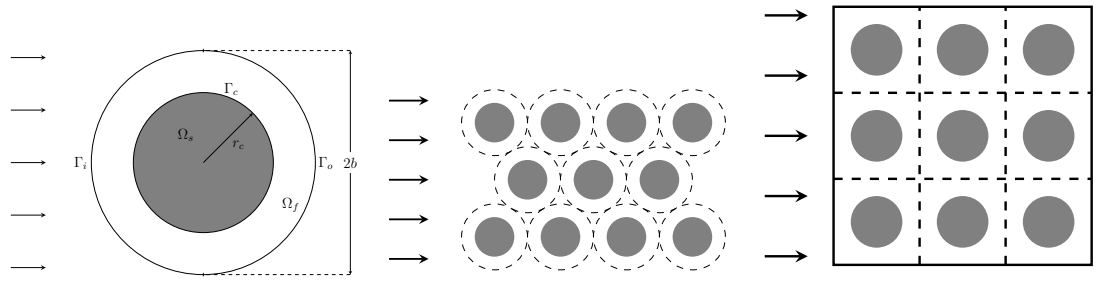

Fig. 1.3 Cell and fluid envelope in Happel's sphere-in-cell model (left) and corresponding hexagonal package (middle), highlighting the presence of voids in the microstructural domain. Cubic packing of cells in the case of spherical cells (right).

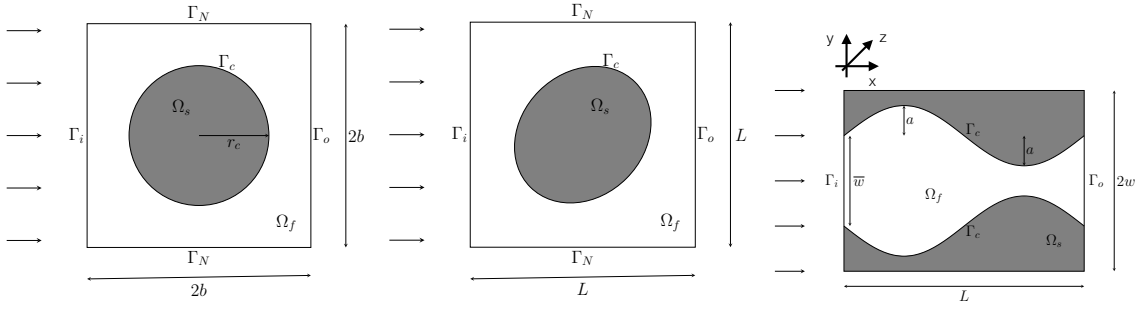

Fig. 1.4 Two-dimensional projection in the $x-y$ plane of the unit spherical cell with cubic packing (left) and two-dimensional projection in the $x-y$ plane of the unit ellipsoidal cell with cubic packing (middle). On the right we show the two-dimensional projection in the $x-y$ plane of the sinusoidal pore (obtained by rotation invariance around the x axis) and the sinusoidal layer (translational symmetry with respect to the z axis).

representative of the real biological microstructure, since there is no package of single spherical Happel's elements which allows to fill the whole microstructured domain, as sketched in Fig.1.3(right). Consequently, the porosity of the medium is not the same as the one of the single microscopic domain.

Our modelling approach considers a cubic packing, as sketched Fig. 1.3 (right), for which the definition of porosity is kept consistent between the microscopic and the macroscopic level. Since an analytic solution of Stokes equation is not available here, we first numerically solved the problem for the elementary cubic cell. Secondly, we considered two different microscopic geometries, mimicking the particles' absorption onto a cell surface and the extravasation over a capillary lumen. In the former case, we considered a spherical cell (Fig. 1.4 left) and an ellipsoidal cell (Fig. 1.4 middle) with cubic packing. In the latter, we investigated the motion of the nanofluid into a pore, considered both as a sinusoidal channel and a sinusoidal layer, whose two-dimensional projection in the $x-y$ plane is shown in Fig. 1.4 (right). For the sake of clarity, the sinusoidal pore is assumed symmetric for rotations around the x axis, while the sinusoidal layer has a translational symmetry with respect to the z axis. Finally, all the biological parameters implemented in the numerical simulations have been collected in Table 1.1.

Parameter	Description	Value
A_H	Hamaker constant	4×10^{-20} J
T	temperature	310.15 K
d_p	particle diameter	0.1-200 nm
ρ_f	fluid density	997 kg m^{-3}
ρ_p	particle density	1060 kg m^{-3}
η	dynamic fluid viscosity	0.001 kg m^{-1} s^{-1}

Table 1.1 Main biological parameters used in the numerical simulations.

1.2.2 Upscaling method

Assuming that the porous tissue is homogeneous and composed by a periodic array of identical unit cells, we can relate the macroscopic model to the microscopic one, and in particular the local deposition rate coefficient k_f to the single cell efficiency η_s. Following [46] we adopt the following relation between k_f and η_s

$$k_f = -\frac{u_x}{L_d} \ln(1 - \eta_s), \tag{1.18}$$

where L_d is the length of the microscopic domain and u_x is the fluid velocity in the principal direction of flow (assumed to be constant, obtained for example by averaging the flow field over the unit cell).

1.2.3 Numerical methods

For the solution of the Langevin equation (1.8) we used a Lattice Kinetic Monte Carlo method with a fixed uniform Cartesian grid. This approach exploits the high dilute assumption for the nanofluid and allows very efficient parallel simulation of particle trajectories due to the possibility to precompute all transition rates between lattice sites. The crucial aspect of the algorithm design is a suitable selection of transition times [50] that allows to avoid undesirable effects well known in the literature [22]. The continuum model (1.9) has been numerically solved by a Finite Volume Method which combines Exponential Fitting for stabilization in case of dominant advection with the technique of [45], which allows to construct 3D control volumes that enforce a Discrete Maximum Principle. The velocity field appearing both in the discrete stochastic model of equation (1.8) and in the continuum model (1.9) has been calculated by a Finite Element solver for Stokes' equation based on the MINI algorithm of [4]. The implementation of the LKMC and FVM algorithms was performed based on in-house C++ libraries [1, 2], while the Stokes solver was implemented in python using the DOLFIN library [37].

1.2.4 Numerical results

The numerical simulation of our multi-scale model investigate the effect of nanoparticles and tissue properties on the single cell absorption efficiency at the microscopic level and the consistency of the upscaling method at the macroscopic scale.

1.2.4.1 Sensitivity analysis of microscopic effects

The many factors that affect the motion of the nanoparticles in the extracellular space at the microscopic level can be separately considered and evaluated in a numerical simulation. In Fig. 1.5, we show the effect of the hydrodynamic retardations on the single cell absorption efficiency: the results obtained for the Happel's sphere-in-cell model and the sinusoidal pore are compared. In both cases, the retardation reduces the single cell efficiency for all particles sizes, with a more significant difference arising for bigger nanoparticles.

In Fig. 1.6, the influence of each of the microscopic forces acting on the nanoparticles is reported. We can see that the effect of the lift force is almost negligible in the low Reynolds number regime of interest to our application, so that the most relevant contribution is given by the van der Waals force. Since the van der Waals force is always attractive, we calculate a growth of the absorption efficiency, which increases with the nanoparticle size.

1.2.4.2 Nanofluid motion around a cell

The motion of the nanofluid in the first system model influences the particle absorption onto a cell surface. We have compared the results for the Happel's sphere-in-cell model, obtained through simulations with the Monte Carlo method and the Finite Volume Method, with RT [48] and TE [58] semi-analytical correlations, versus the results presented in [55]. In Fig. 1.7, we report the absorption efficiency versus the nanoparticle diameter, showing that the cell efficiency decreases with increasing particle size. As expected, the effect of diffusion becomes smaller and the nanoparticles deviate less from the streamlines of the fluid flow. We remark that our numerical simulations yield a higher cell efficiency with respect to the literature values, except for the smaller particles.

Secondly, we have investigated the effect of the microscopic geometry on the single cell absorption efficiency, taking into account the more realistic cubic packing of the cubic unit cell. Since the efficacy of the FVM model has been validated against the MC one, we only consider the continuum approach. Then, we have first numerically computed the fluid velocity in the representative cubic domain solving Stokes equation (1.7) and then we have solved equation (1.9) for the nanoparticle concentration by applying a Finite Volume Method. We have compared the single cell efficiency obtained through the Happel sphere-in-cell model against the case of a spherical cell with cubic packing with r_c and b fixed and different values of porosity. Let us highlight that the minimum allowed porosity in the case of spherical cells with cubic packing is larger than in the case of Happel's model. Fig. 1.8 shows that η_s is smaller for a sphere with cubic packing than for the Happel's model.

Thirdly, we have compared the efficiency of a single spherical cell with an ellipsoidal cell with cubic packing at fixed porosity $\varepsilon = 0.6649$. The resulting curves of single cell absorption efficiency as a function of the nanoparticle size are plotted in Fig. 1.9. In both cases the cell efficiency decreases for increasing particle size, being almost the same for the smallest nanoparticles. For the spherical cell, the efficiency also increases for increasing nanoparticle size.

1.2.4.3 Nanofluid motion into a pore/layer

Now let us consider the nanofluid motion into either a sinusoidal pore or a sinusoidal layer. As in the previous analysis, we have first numerically computed the fluid velocity, i.e. by solving equation (1.7), and then we calculated the nanoparticle concentration through the solution of equation (1.9). In Fig. 1.10 we depict

the single cell efficiency in the case of a sinusoidal pore and a sinusoidal layer at fixed porosity and fixed tortuosity τ, defined as the ratio between the amplitude a of the sinusoidal and the corresponding wavelength L. We find that the sinusoidal pore has a bigger cell efficiency for all the particles sizes under consideration. The effect of tortuosity on the cell efficiency is shown in Fig. 1.11 for both the sinusoidal pore and the sinusoidal layer. We set $\tau = 0.1, 0.2$ for the sinusoidal layer and $\tau = 0.1, 0.2, 0.3$ for the sinusoidal pore: in both cases, the efficiency decreases for decreasing tortuosity.

1.3 A macro-scale approach to transport in vascularized tissues

Microvascular fluid dynamics plays a fundamental role in determining the efficiency of the drug delivery of nanoparticles. In this section we study the flow in the capillary network coupled with interstitial filtration, see equation (1.19), and transport of particles described by equation (1.20). As sketched in Figure 1.12, flow in microvessels, interstitial flow and transport are coupled phenomena to be modeled by space-time dependent partial differential equations, which can be efficiently solved using advanced numerical technique, like the *embedded multiscale method*, developed in [17, 18] and later applied in [10, 11] for studying perfusion and drug delivery.

The geometrical configuration of the macro-scale model is shown in Figure 1.12: a tumor slab of R3230AC mammary carcinoma on a rat model, whose data are reported in [52] and made available as a result of the Microcirculation Physiome Project [44]. The tumor slab size is $220 \times 208 \times 92\ 10^{-5}$ m and it contains 105 different segments with radii spanning from 5.5×10^{-6} m to 33.2×10^{-6} m. The variability in the radius introduces several technical difficulties in the mathematical model; for example the enforcement of mass conservation at each bifurcation of the network has not yet been addressed in the available computational solver. For this reason, we adopt here a constant radius $R = 7.64 \times 10^{-6}$ m that is the arithmetic average of the individual radii of each segment. A generalization of the flow model to varying capillary radius is presented in [42] and will be used in forthcoming studies.

The computational model is decomposed into the microvascular network Λ and the surrounding malignant tissue Ω. The subscript v (vascular) will denote all the variables defined in the capillary domain, while the subscript t labels the tissue. Our computations simulate a protocol for HCT where the tumor slab is infused with a solution of particles. The injected particles enter the (virtual) tumor model through the inlets of the capillary network. These inlets are represented by the specific points of the capillaries intersecting with the chosen faces of the tumor slab.

The physical quantities of interest are the flow pressure p, the velocity $\mathbf{u}$ and the concentration of transported solutes c. All fields depend on time t and space, $\mathbf{x} \in \Omega$ being the spatial coordinates. The mathematical model stems from fundamental balance laws regulating the flow in the capillary bed, the extravasation of plasma and solutes and their transport in the interstitial tissue.

1.3.1 Governing equations of flow at the macroscale

The flow model includes two components, i.e. the microcirculation and the flow in the interstitial tissue, coupled by interface conditions at the microvascular wall, behaving as a semipermeable membrane. The malignant interstitial volume is assumed to be an isotropic porous material, where the flow obey the Darcy's law.

Microcirculation is characterized by low Womersley and Reynolds numbers [6, 8, 53]. In these conditions, the Navier-Stokes equations reduce to steady Stokes flow. Under additional assumptions of (*i*) straight channels, (*ii*) rigid walls (*iii*) and constant radius, (*iv*) no-slip boundary conditions for the velocity, (*v*) absence of body forces such as gravity and inertial forces, Poiseuille flow can be exactly integrated, namely (1.19e). As discussed in [8, 23, 24, 51], although assuming Poiseuille flow considerably reduces the computational cost, some assumptions do not fully apply in the present context. Indeed, deviations must be small: if transmural flow occurs, it has to be small with respect to the axial component of the velocity; each vessel branch does not have to be straight, but only a small curvature is allowed. Improvements of the current flow model are in order: (*a*) for a better approximation of the extravasation effects; (*b*) to relieve constraints on small curvature and consequently allow to analyze configurations characterized by high tortuosity, which plays an important role on the average hydraulic conductivity of tumors, as discussed in [47]; (*c*) to improve the characterization of stresses on the wall, which in turn will affect particle adhesion.

The arc length coordinate along each capillary segment is represented by the symbol s, while λ denotes the reference vector that characterizes the segment orientation. Furthermore, we follow [7, 54] to model the lymphatic drainage.

The coupled mathematical model for microcirculation and flow in interstitial volume allows to find the pressure p_t, p_v and the velocity fields $\mathbf{u}_t$, $\mathbf{u}_v$ such that the flow problem is:

$$-\nabla\cdot\left(\frac{\kappa}{\mu}\nabla p_t\right)+L_p^{LF}\frac{s}{v}(p_t-p_L)-f_b(\overline{p}_t,p_v)\delta_\Lambda=0\,,\qquad \text{in}\,\Omega\,,\tag{1.19a}$$

$$\mathbf{u}_t=-\frac{\kappa}{\mu}\nabla p_t\,,\qquad \text{in}\,\Omega\,,\tag{1.19b}$$

$$-\frac{\pi R^4}{8\mu}\frac{\partial^2 p_v}{\partial s^2}+f_b(\overline{p}_t,p_v)=0\,,\qquad s\in\Lambda\,,\tag{1.19c}$$

$$f_b(\overline{p}_t,p_v)=2\pi RL_p((p_v-\overline{p}_t)-\sigma^p(\pi_v^p-\pi_t^p))\,,\qquad \text{in}\,\Lambda\,,\tag{1.19d}$$

$$\mathbf{u}_v=-\frac{R^2}{8\mu}\frac{\partial p_v}{\partial s}\lambda\,,\qquad s\in\Lambda\,,\tag{1.19e}$$

$$-\frac{\kappa}{\mu}\nabla p_t\cdot\mathbf{n}=\beta_b(p_t-p_0)\,,\qquad \text{on}\,\partial\Omega\,.\tag{1.19f}$$

where $\overline{p}_t$ represents an average of the interstitial pressure acting on the capillary surface, namely

$$\overline{p}_t(s)=\frac{1}{2\pi R}\int_0^{2\pi}p_t(s,\theta)Rd\theta\,,$$

being θ the angular coordinate on the cylindrical surface representing the capillary wall.

We have imposed a pressure gradient along the capillary vessels. Since both the inflow and outflow of the capillary vessels are located on the outer edges of the slab, we enforced a known pressure p_{in} on two neighbor inlet, whereas outlet pressure p_{out} is assigned on the opposite faces. The pressure drop between inlets and outlets is calibrated according to the following argument. Given an estimate of the average blood velocity in the capillary circulation, equal to 0.1 mm/s according to the data provided by [34], we use Poiseuille's law to calculate the corresponding pressure drop. More precisely, we have applied a fictitious model consisting of

a straight rigid pipe of length $|\Lambda|$ and radius R, to calculate the pressure drop $p_{in} - p_{out}$ that corresponds to a velocity of 0.1 mm/s in the pipe. We have imposed the Robin-type boundary conditions (1.19f) for the blood flow in the interstitial volume. In this equation, p_0 stands for the far field pressure value, while β_b denotes an effective flow conductivity accounting for the tissue layers surrounding the tumor slab.

Let L_p be the hydraulic permeability of the vessel wall (see Table 1.3.2 for units and physiological values) and let $p_v - \overline{p}_t$ be the pressure difference between the vessels and the interstitial volume. Because of osmosis, the pressure drop across the capillary wall is a function of difference in chemical potential of the chemicals soluted in blood, [15, 26]: this determines the oncotic pressure jump $(\pi_v^p - \pi_t^p)$ modulated by the sieving coefficient σ^p. The oncotic pressure is defined as $\pi = R_g T c$, where c is the concentration of a given osmotic agent, R_g is the universal gas constant and T stands for the absolute temperature. The coefficient σ^p accounts for the difference of a semipermeable membrane compared to the case of ideal permeability (i.e., no resistance force on the molecules passing through the membrane). It spans from 0 to 1, where small values characterize ideal membranes, while larger values are typical of selective filters.

Proteins dissolved into the blood serum, and albumin in particular, are responsible for most of the oncotic pressure generated in the capillaries, which in physiological conditions is about 25 mmHg. To model this effect we set $\pi_v^p = 25$, $\pi_t^p = 0$ mmHg and $\sigma^p \simeq 1$, since proteins hardly leak through the capillary walls. As a result we obtain $\sigma^p(\pi_v^p - \pi_t^p) = 25$ mmHg (1 mmHg = 133.322 Pa). The oncotic effect generated by the injected VMNs is neglected in this work. Nevertheless, this is an open question to be explored in future studies, since albumin serum concentration is only 5 to 10 times bigger than the VMN systemic concentrations reached after injection.

In order to model the capillary phenotype typically observed in tumors, we increase the magnitude of the hydraulic permeability as in [7], such that the model will account of the well known enhanced permeability and retention effect (EPR). To balance leakage of arterial capillaries, venous and lymphatic systems absorb the fluid in excess. For the sake of generality, we include lymphatic drainage in the model, although the lymphatic system may be disfunctional in tumors. Following [7, 54], we model them as a distributed sink term in the interstitial volume. It is assumed that the volumetric flow rate due to lymphatic vessels, Φ^{LF}, is proportional to the pressure difference between the interstitium and the lymphatics, namely $\Phi^{LF}(p_t) = L_p^{LF} \frac{s}{v}(p_t - p_L)$, where L_p^{LF} is the hydraulic permeability of the lymphatic wall, s/v is the surface area of lymphatic vessels per unit volume of tissue and p_L is the hydrostatic pressure within the lymphatic channels.

1.3.2 Governing equations of mass transport at the macroscale

Mass transport in the capillary bed is modelled by means of advection-diffusion equations. As shown in [16], a one dimensional model for mass transport in the capillaries network can be derived starting from the 3D advection-diffusion problem. The coupled problem, accounting for transport of chemicals from the microvasculature to the interstitium, dictates the evolution of the concentrations c_v and c_t respectively.

In the interstitial tissue the particles or molecules are advected by the fluid and diffuse in all Ω. In addition they may be metabolised by the cells in the interstitial tissue. The distribution of solutes in the interstitial tissue is also affected by the lymphatic drainage. According to the assumptions at the basis of the flow model, the effect of lymphatic drainage on mass transport is represented as a distributed sink proportional to $L_p^{LF} \frac{s}{v}(p_t - p_L)c_t$.

Given this notation and assumptions, the mass transport model at the macroscale reads as follows:

$$\frac{\partial c_v}{\partial t}+\frac{\partial}{\partial s}\left((\mathbf{u}_v\cdot\lambda)c_v-D_v\frac{\partial c_v}{\partial s}\right)=-\frac{1}{\pi R^2}f_c(\overline{p}_t,p_v,\overline{c}_t,c_v), \qquad \text{in } \Lambda\times(0,t), \tag{1.20a}$$

$$f_c(\overline{p}_t,p_v,\overline{c}_t,c_v)=2\pi R\big[L_p((p_v-p_t)-\sigma^p(\pi_v^p-\pi_t^p))c_v+P(c_v-c_t)\big], \qquad \text{in } \Lambda, \tag{1.20b}$$

$$\frac{\partial c_t}{\partial t}+\nabla\cdot(c_t\mathbf{u}_t-D_t\nabla c_t)+L_p^{LF}\frac{s}{v}(p_t-p_L)c_t+k_fc_t=f_c(\overline{p}_t,p_v,\overline{c}_t,c_v)\delta_\Lambda, \qquad \text{in } \Omega\times(0,t), \tag{1.20c}$$

$$\big(c_t\mathbf{u}_t-D_t\nabla c_t\big)\cdot\mathbf{n}=\beta_c c_t, \qquad \text{on } \partial\Omega\times(0,t) \tag{1.20d}$$

where D_v and D_t are the particle diffusivities, in the capillaries and the interstitium, respectively, assumed to be constant in each region. The rate of metabolization in the interstitium is denoted by k_f and, as an instance for many other parameters, can be calculated on the basis of the microscale model illustrated above. Unfortunately, simulations for a specific class of nanoparticles where the macroscopic model is informed by the microscale are not yet available but will be the result of work in progress based on the general framework proposed here.

We describe the capillary walls as *semipermeable membranes* allowing leakage of fluid and selective filtration of molecules. Again, the Kedem-Katchalsky equations represent a good model for these phenomena [26]. Then, under the assumption that capillaries can be modeled as cylindrical channels, the magnitude of the mass flux exchanged per unit length between the network of capillaries and the interstitial volume at each point of the capillary vessels is

$$f_c(\overline{p}_t,p_v,\overline{c}_t,c_v)=2\pi R\big[(1-\sigma)J_b(\overline{p}_t,p_v)c_v+P(c_v-\overline{c}_t)\big].$$

We posit that a constant concentration of particles, denoted by c_{inj}, is available in the blood flowing into the slab through the inflow sections of the vasculature. The particles are free to leave the system through the complementary outflow boundaries. At the initial time the vascular network and the tumor slab do not contain particles. For closing the transport problem, we model the layers of tissue surrounding the tumor sample by means of a condition that prescribes the flow resistance due to the outer layers of tissue, namely equation (1.20d).

Table 1.2 Parameters and data for mass and thermal transport.

Symbol	Parameter	Units	Value	Source	Eqn.
L_p	Hydraulic permeability, capillary wall	$(m^2.s)/kg$	10^{-10}	[10]	(1.20b)
$L_p^{LF}\frac{s}{v}$	Effective permeability, Lymphatic Vessels	$(mmHg\ hour)^{-1}$	0.5	[10]	(1.20c)
c_{inj}	Inflow particle concentration	gr/m^3	1425.9	[10]	–
d	Edge length of particles	m	1×10^{-8}	[12]	–
m	Mass of particles	gr	8×10^{-18}	[12]	–
D_v	Vascular diffusivity of particles	m^2/sec	9.0687×10^{-11}	[10]	(1.20a)
D_t	Interstitial diffusivity of particles	m^2/sec	1.2955×10^{-11}	[10]	(1.20c)
P	Vascular permeability of particles	m/sec	2×10^{-6}	[10]	(1.20b)

1.3.3 Computational solver

The discretization of problems (1.19) and (1.20) is performed by using the finite element method. After partitioning the tumor and vasculature domains, Ω and Λ respectively, into elements, (see Figure 1.12 top right panel showing a representative computational domain of only 32624 tetrahedral elements) the solution of the governing equations are approximated with piecewise polynomial functions in the framework of the variational formulation. In particular, piecewise linear finite elements are used for all the unknowns, namely p_t, c_t and p_v, c_v, on a computational grid consisting of 49655 grid points and 272872 tetrahedral elements. Velocities $\mathbf{u}_t, \mathbf{u}_v$ are reconstructed in the post-processing phase using the pressure fields. We have adopted the GMRES method with incomplete-LU preconditioning to solve the algebraic systems following from the finite element discretization. The sensitivity of the results with respect to the mesh size has been tested and mesh independence is shown for grids finer than 257109 elements.

The domains Ω and Λ feature heterogeneous dimensionality. The former is 3D, the latter is 1D. In order to model the natural leakage of capillaries, we apply the *embedded multiscale method* [18, 17, 10, 11], where the capillary bed is represented as a network of one-dimensional channels acting as concentrated sources of mass for the interstitial volume. The main advantage of the proposed scheme is that the computational grids required to approximate the equations on the capillary network and on the interstitial volume are completely independent. As a result, arbitrarily complex microvascular geometries can be studied with modest computational effort. From the standpoint of numerical approximation, the theoretical aspects of the method have been addressed in the works by D'Angelo [18, 17]. These algorithms have been implemented using GetFem++, a general C++ finite element library [49].

1.3.4 Numerical simulations

A standard protocol for nano-based cancer treatment is not yet available. We have performed virtual experiments using data from previous studies that target nano-based tumor hyperthermia [36, 39, 57]. On the basis of these examples, we analyze a time interval of 60 minutes, where for the initial 40 minutes the tumor is supplied with a solution of particles, idellay provided by an intravascular injection of particles. The underlying assumption is that, for a small animal, the intravenous infusion of a nano-fluid generates an initial homogeneous concentration in the entire systemic circulation, which we denote as c_{inj}. In particular, we have chosen to run experiments targeting the reference value $c_{ref} = 1$ mg/ml because it matches the injected concentrations used in the experiments of [12]. We use the computational model to perform the following studies: (i) an analysis of average particle concentration time-course during injection whose results are reported in Figure 1.13; (ii) combined spatial maps of interstitial fluid pressure, concentration and temperature. In particular, Figure 1.14 shows particle concentration field at at 40 min., the time when particle injection is switched off.

In Figure 1.13, the mass density of particles delivered to the tumor slab is shown. In these simulations the injected particle density has been set to match reference slab concentration of 1 mg/ml. Two characteristic traits of small-particle delivery emerge. Figure 1.13 shows the delivery efficiency, namely the mass of delivered particles per unit mass of delivered material. More precisely we plot,

$$\frac{\int_\Omega c_t dx + \int_\Lambda \pi R^2 c_v ds}{\int_0^T \left(\pi R^2 c_{inj} \mathbf{u}_{in} \cdot \lambda\right) dt}. \tag{1.21}$$

We observe that more than 50% of the injected particles are absorbed by the tumor slab, because of their ability to extravasate and diffuse within the interstitial volume. However, for similar reasons, small particles suffer from small residence times, as demonstrated by the quick drop of particle concentration and temperature after 40 min. In other words, the particle concentration significantly drops as soon as particle injection is switched off.

For the same simulations, particle concentration and temperature fields are shown in Figure 1.14. For a highly vascularized small tumor (about 0.5 mm width) the particle distribution among the tissue is rather uniform.

1.4 Conclusions and future perspectives

In this work we have proposed a multi-scale mathematical model for the description of the diffusion, transport and absorption of nanoparticles in living tissues. In particular, using a bottom-up approach, the upscaling technique introduced allows to determine the absorption rate of nanoparticles in a continuous macroscopic model, resulting in a one-way coupling between micro- and macro-scales.

We have addressed microscale simulations first. We have implemented a discrete and a continuous microscopic models in two representative geometries, mimicking both the absorption rate in a regular packing of cellular aggregates and the nanoparticle extra-vasation through the sinusoidal surface of a pore/layer. The corresponding microscopic models account for the presence of hydrodynamic retardations and driving forces, namely the lift and the Wan der Waals interaction forces, and they have been solved using Kinetic Monte Carlo and the Finite Volume methods, respectively. The results of the microscopic numerical simulations allowed to analyze the effects of the different physical factors acting on a nanoparticle on the cell efficiency. In the case of a cellular absorption, we have proposed a more realistic cubic packing for both a spherical and a ellipsoidal unit cell, showing that the absorption efficiency deviates significantly from the previous results obtained using idealized Happel's model, therefore we remark that a numerical approach is required to properly identify the local absorption parameter since the analytical simplification can drive to results that are off by as much as 20%.

We have also found that both the hydrodynamic retardations and the van der Waals interaction forces influence the single cell efficiency, although with opposite effects. Similar results are found also for the pore/layer geometry mimicking the extravasation process, where the cell efficiency is strongly dependent of the surface tortuosity.

In conclusion, we have demonstrated that the transport of nanoparticles in living tissues is strongly affected by the geometrical and the multi-physical factors at the microscale. Therefore, the results of this work push towards the development of a more accurate microscopic models in order to improve the level of approximation at which the transport properties across the scales must be investigated. Although we have validated the upscaling technique of the proposed multi-scale approach, future refinements would take into account other relevant physical phenomena. For example, other driving forces at the microscale should be considered, such as the electrostatic potential deriving from surface functionalization [3] or from the protein corona which inevitably forms on a nanoparticle's surface in a biological medium [38].

At the macroscale level, we have outlined new mathematical model designed to investigate the coupled flow and mass transfer at the level of the whole tumor. Basic balance and constitutive laws have been adopted to simulate the interactions among the main compartments of the tumor tissue. The main contribution of the computational framework is that flow and mass transfer in the capillary and interstitial medium are coupled for simulations performed using a microvasculature configuration based on physiological data. The

simulations suggest that network topology and particle distribution along the microvasculature are the key factors in particle delivery approach, especially in the cases characterized by hindered particle extravasation.

One of the main limitations of the macroscopic approach is the difficulty of determining the model parameters. Table 1.3.2 lists the most significant ones, such as the hydraulic permeability of the capillary walls, the particle diffusivity tensor in the blood stream and in the tissue matrix, the vascular permeability of particles and the deposition rate coefficient. All these coefficients are usually estimated from available literature sources based on experimental data or phenomenological models. The corresponding values are affected by large uncertainties. For any specific family of nanoparticles, a mechanistic approach, as the one developed here at the microscale, would bring huge benefits in reducing the margins of error with respect of the parameter values. Here, we have outlined the application of this approach to the estimate of the deposition rate coefficient, but the general methodology find ubiquitous applications to improve the reliability of macroscale simulations, which root in this preliminary investigation and will be surely at the core of future research efforts.

Acknowledgements We would thank Stefania Lunardi for the help in collecting the information presented in the introductory part and her contribution in the numerical simulations with the LKMC technique for the microscopic model, Michele Pollini for the help in conducting the FE continuum simulations for the microscopic model and Dr. Elena Danesi for the help in both the aspects covered by Stefania and Michele as co-supervisor of their master thesis.

References

1. (2016). URL https://redmine.mate.polimi.it/projects/bim.
2. (2016). URL https://redmine.mate.polimi.it/projects/lkmc
3. Albanese, A., Tang, P., Chan, W.: The effect of nanoparticle size, shape, and surface chemistry on biological systems. Ann. Rev. Biomed. Eng. **14**(1) (2012)
4. Arnold, D., Brezzi, F., Fortin, M.: A stable finite element for the stokes equations. CALCOLO **21**(4), 337–344 (1984)
5. Banerjee, R.K., van Osdol, W.W., Bungay, P.M., Sung, C., Dedrick, R.L.: Finite element model of antibody penetration in a prevascular tumor nodule embedded in normal tissue. Journal of controlled release **74**(1), 193–202 (2001)
6. Baxter, L., Jain, R.: Transport of fluid and macromolecules in tumors. i. role of interstitial pressure and convection. Microvascular Research **37**(1), 77–104 (1989)
7. Baxter, L., Jain., R.: Transport of fluid and macromolecules in tumors ii. role of heterogeneous perfusion and lymphatics. Microvascular Research **40**(2), 246–263 (1990)
8. Blake, T., Gross, J.: Analysis of coupled intra- and extraluminal flows for single and multiple capillaries. Mathematical Biosciences **59**(2), 173–206 (1982)
9. Carmeliet, P., Jain, R.: Angiogenesis in cancer and other diseases. Nature **407**(6801), 249–257 (2000)
10. Cattaneo, L., Zunino, P.: A computational model of drug delivery through microcirculation to compare different tumor treatments. International Journal for Numerical Methods in Biomedical Engineering **30**(11), 1347–1371 (2014)
11. Cattaneo, L., Zunino, P.: Computational models for fluid exchange between microcirculation and tissue interstitium. Networks and Heterogeneous Media **9**(1), 135–159 (2014)
12. Cervadoro, A., Giverso, C., Pande, R., Sarangi, S., Preziosi, L., Wosik, J., Brazdeikis, A., Decuzzi, P.: Design maps for the hyperthermic treatment of tumors with superparamagnetic nanoparticles. PLoS ONE **8**(2) (2013)
13. Cherukat, P., McLaughlin, J.B.: The inertial lift on a rigid sphere in a linear shear flow field near a flat wall. Journal of Fluid Mechanics **263**, 1–18 (1994)
14. Chou, C.Y., Huang, C.K., Lu, K.W., Horng, T.L., Lin, W.L.: Investigation of the spatiotemporal responses of nanoparticles in tumor tissues with a small-scale mathematical model. PloS one **8**(4), e59,135 (2013)
15. Curry, F.: Hand Book of Physiology, chap. 8 Mechanics and thermodynamics of transcapillary exchange, pp. 309–374. Am. Physiol. Soc. (1984)
16. D'Angelo, C.: Multiscale modeling of metabolism and transport phenomena in living tissues. Ph.D. thesis, Politecnico di Milano (2007)

17. D'Angelo, C.: Finite element approximation of elliptic problems with dirac measure terms in weighted spaces: Applications to one- and three-dimensional coupled problems. SIAM Journal on Numerical Analysis **50**(1), 194–215 (2012)
18. D'Angelo, C., Quarteroni, A.: On the coupling of 1d and 3d diffusion-reaction equations. application to tissue perfusion problems. Mathematical Models and Methods in Applied Sciences **18**(8), 1481–1504 (2008)
19. Decuzzi, P., Ferrari, M.: The role of specific and non-specific interactions in receptor-mediated endocytosis of nanoparticles. Biomaterials **28**(18), 2915–2922 (2007)
20. Decuzzi, P., Ferrari, M.: The receptor-mediated endocytosis of nonspherical particles. Biophysical journal **94**(10), 3790–3797 (2008)
21. Elimelech, M.: Particle deposition on ideal collectors from dilute flowing suspensions: Mathematical formulation, numerical solution, and simulations. Separations Technology **4**(4), 186–212 (1994)
22. Flamm, M.H., Diamond, S.L., Sinno, T.: Lattice kinetic monte carlo simulations of convective-diffusive systems. the journal of chemical physics (130), 094,904 (2009)
23. Fleischman, G., Secomb, T., Gross, J.: The interaction of extravascular pressure fields and fluid exchange in capillary networks. Mathematical Biosciences **82**(2), 141–151 (1986)
24. Flieschman, G., Secomb, T., Gross, J.: Effect of extravascular pressure gradients on capillary fluid exchange. Mathematical Biosciences **81**(2), 145–164 (1986)
25. Florence, A.T.: "targeting" nanoparticles: the constraints of physical laws and physical barriers. Journal of Controlled Release **164**(2), 115–124 (2012)
26. Friedman, M.: Principles and Models of Biological Transport. Springer, New York (2008)
27. Gao, Y., Li, M., Chen, B., Shen, Z., Guo, P., Wientjes, M.G., Au, J.L.S.: Predictive models of diffusive nanoparticle transport in 3-dimensional tumor cell spheroids. The AAPS journal **15**(3), 816–831 (2013)
28. Goldman, A., Cox, R., Brenner, H.: Slow viscous motion of a sphere parallel to a plane wall–ii couette flow. Chemical engineering science **22**(4), 653–660 (1967)
29. Goldman, A., Cox, R.G., Brenner, H.: Slow viscous motion of a sphere parallel to a plane wall–i motion through a quiescent fluid. Chemical engineering science **22**(4), 637–651 (1967)
30. Goodman, T.T., Chen, J., Matveev, K., Pun, S.H.: Spatio-temporal modeling of nanoparticle delivery to multicellular tumor spheroids. Biotechnology and bioengineering **101**(2), 388–399 (2008)
31. Graff, C.P., Wittrup, K.D.: Theoretical analysis of antibody targeting of tumor spheroids importance of dosage for penetration, and affinity for retention. Cancer research **63**(6), 1288–1296 (2003)
32. Hanahan, D., Weinberg, R.: The hallmarks of cancer. Cell **100**(1), 57–70 (2000)
33. Hicks, K., Pruijn, F., Secomb, T., Hay, M., Hsu, R., Brown, J., Denny, W., Dewhirst, M., Wilson, W.: Use of three-dimensional tissue cultures to model extravascular transport and predict in vivo activity of hypoxia-targeted anticancer drugs. Journal of the National Cancer Institute **98**(16), 1118–1128 (2006)
34. Intaglietta, M., Silverman, N., Tompkins, W.: Microvascular research. Capillary flow velocity measurements in vivo and in situ by television methods **10**(2), 165–179 (1975)
35. Israelachvili, J.N.: Intermolecular and surface forces: revised third edition. Academic Press (2011)
36. Johannsen, M., Gneveckow, U., Eckelt, L., Feussner, A., Waldner, N., Scholz, R., S. Deger andP. Wust, S.L., Jordan, A.: Clinical hyperthermia of prostate cancer using magnetic nanoparticles: Presentation of a new interstitial technique. International Journal of Hyperthermia **21**(7), 637–647 (2005)
37. Logg, A., Wells, G.N.: Dolfin: Automated finite element computing. ACM Trans. Math. Softw. **37**(2), 20:1–20:28 (2010)
38. Monopoli, M., Bombelli, F.B., Dawson, K.: Nanobiotechnology: Nanoparticle coronas take shape. Nature Nanotech **6** (2011)
39. Mornet, S., Vasseur, S., Grasset, F., Duguet, E.: Magnetic nanoparticle design for medical diagnosis and therapy. Journal of Materials Chemistry **14**(14), 2161–2175 (2004)
40. Nelson, K.E., Ginn, T.R.: Colloid filtration theory and the happel sphere-in-cell model revisited with direct numerical simulation of colloids. Langmuir **21**(6), 2173–2184 (2005)
41. Norris, E., King, J.R., Byrne, H.M.: Modelling the response of spatially structured tumours to chemotherapy: Drug kinetics. Mathematical and Computer Modelling **43**(7), 820–837 (2006)
42. Notaro, D., Cattaneo, L., Formaggia, L., Scotti, A., Zunino, P.: A mixed finite element method for modeling the fluid exchange between microcirculation and tissue interstitium. In: Advances in Discretization Methods, SEMA-SIMAI Springer Series (to appear, 2016)
43. van Osdol, W., Fujimori, K., Weinstein, J.N.: An analysis of monoclonal antibody distribution in microscopic tumor nodules: consequences of a"binding site barrier". Cancer research **51**(18), 4776–4784 (1991)
44. Popel, A., Greene, A., Ellis, C., Ley, K., Skalak, T., Tonellato, P.: The microcirculation physiome project. Annals of Biomedical Engineering **26**, 911–913 (1998)

45. Putti, M., Cordes, C.: Finite element approximation of the diffusion operator on tetrahedra. SIAM Journal on Scientific Computing **19**(4), 1154–1168 (1998)
46. Quintard, M., Whitaker, S.: Aerosol filtration: An analysis using the method of volume averaging. Journal of aerosol science **26**(8), 1227–1255 (1995)
47. R. Penta, D.A.: The role of the microvascular tortuosity in tumor transport phenomena. J. Theoret. Biol. **364**, 80–97 (2015)
48. Rajagopalan, R., Tien, C.: Trajectory analysis of deep-bed filtration with the sphere-in-cell porous media model. AIChE Journal **22**(3), 523–533 (1976)
49. Renard, Y., Pommier, J.: (2012). URL http://download.gna.org/getfem/html/homepage/
50. S., L.: Simulazione microscala dell'efficienza di assorbimento di nanoparticelle per trasporto di farmaco. Master's thesis, Politecnico di Milano (2014)
51. Secomb, T., ans E.Y.H. Park, R.H., Dewhirst, M.: Green's function methods for analysis of oxygen delivery to tissue by microvascular networks. Annals of Biomedical Engineering **32**(11), 1519–1529 (2004)
52. Secomb, T., Hsu, R., Braun, R., Ross, J., Gross, J., Dewhirst, M.: Theoretical simulation of oxygen transport to tumors by three-dimensional networks of microvessels. Advances in Experimental Medicine and Biology **454**, 629–634 (1998)
53. Skalak, R., Keller, S., Secomb, T.: Mechanics of blood flow. Journal of Biomechanical Engineering **103**(2), 102–115 (1981)
54. Soltani, M., Chen, P.: Numerical modeling of interstitial fluid flow coupled with blood flow through a remodeled solid tumor microvascular network. PLoS ONE **8**(6) (2013)
55. Su, D., Ma, R., Salloum, M., Zhu, L.: Multi-scale study of nanoparticle transport and deposition in tissues during an injection process. Medical & biological engineering & computing **48**(9), 853–863 (2010)
56. Taffetani, M., de Falco, C., Penta, R., Ambrosi, D., Ciarletta, P.: Biomechanical modelling in nanomedicine: multiscale approaches and future challenges. Archive of Applied Mechanics **84**(9-11), 1627–1645 (2014)
57. Terentyuk, G., Maslyakova, G., Suleymanova, L., Khlebtsov, N., Khlebtsov, B., Akchurin, G., Maksimova, I., Tuchin, V.: Laser-induced tissue hyperthermia mediated by gold nanoparticles: Toward cancer phototherapy. Journal of Biomedical Optics **14**(2) (2009)
58. Tufenkji, N., Elimelech, M.: Correlation equation for predicting single-collector efficiency in physicochemical filtration in saturated porous media. Environmental science & technology **38**(2), 529–536 (2004)
59. Waite, C.L., Roth, C.M.: Binding and transport of pamam-rgd in a tumor spheroid model: The effect of rgd targeting ligand density. Biotechnology and bioengineering **108**(12), 2999–3008 (2011)
60. Ward, J.P., King, J.R.: Mathematical modelling of drug transport in tumour multicell spheroids and monolayer cultures. Mathematical biosciences **181**(2), 177–207 (2003)
61. Ying, C.T., Wang, J., Lamm, R.J., Kamei, D.T.: Mathematical modeling of vesicle drug delivery systems 2 targeted vesicle interactions with cells, tumors, and the body. Journal of laboratory automation **18**(1), 46–62 (2013)

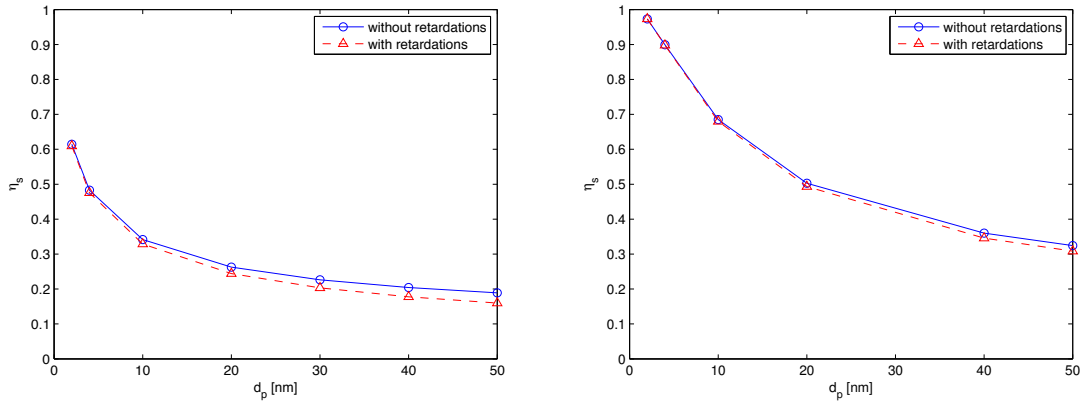

Fig. 1.5 Effect of hydrodynamic retardations on the single cell absorption efficiency, in the case of (a) Happel's sphere-in-cell model, (b) sinusoidal pore with $\tau = 0.2$.

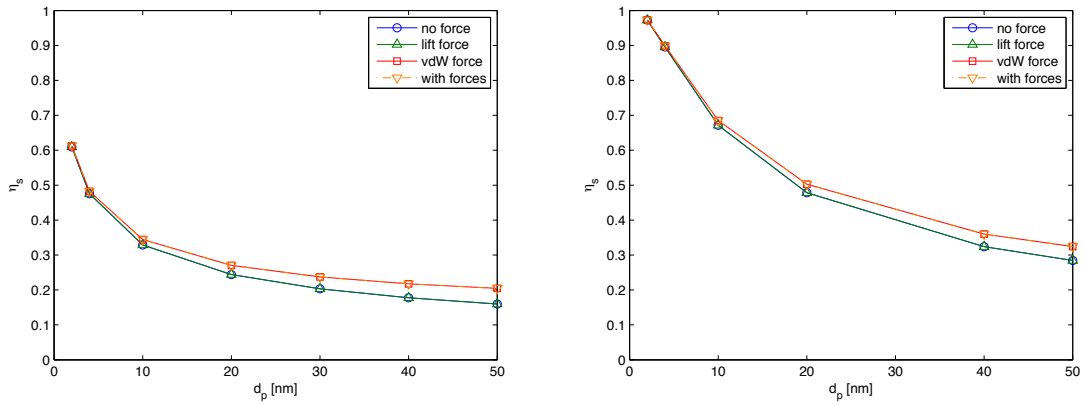

Fig. 1.6 Effect of van der Waals and lift forces on the single cell absorption efficiency, in the case of (a) Happel's sphere-in-cell model, (b) sinusoidal pore with $\tau = 0.2$.

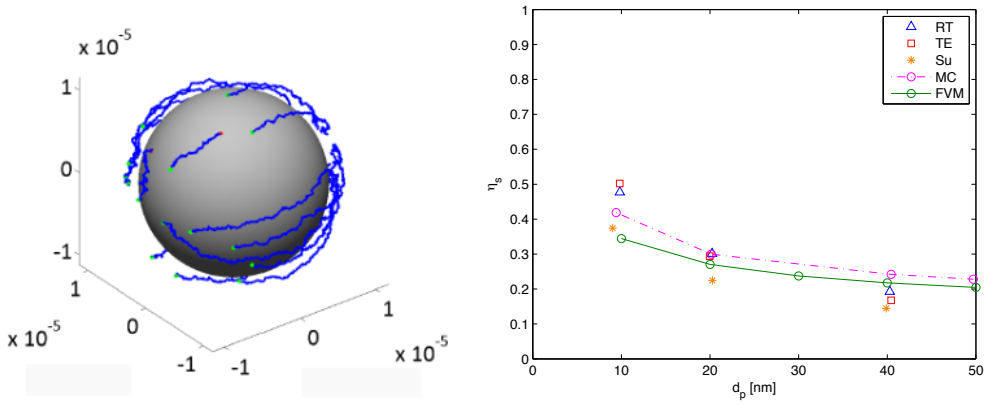

Fig. 1.7 Nanoparticles motion in the fluid layer in Happel's sphere-in-cell model. (a) Nanoparticles trajectories obtained through Monte Carlo simulations; (b) trend of single cell absorption efficiency versus particle size in the case of Happel's sphere-in-cell model. Here RT and TE represent the results of semi-analytical correlations, Su denotes the results in [55], MC and FVM denote the results obtained through our numerical simulations with Monte Carlo method and Finite Volume Method. $r_c = 10\ \mu\text{m}$, $\varepsilon = 0.36$, $U_\infty = 3.7 \cdot 10^{-4}\ \text{m s}^{-1}$.

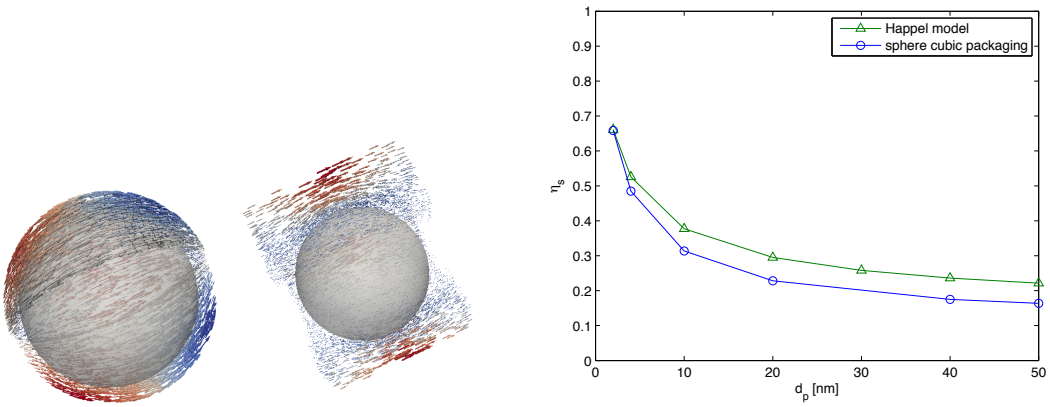

Fig. 1.8 Nanofluid motion around a spherical cell at fixed porosity $\varepsilon = 0.6649$ in the case of Happel's model and our cubic packing. (a) Streamlines of fluid velocity in Happel's sphere-in-cell model; (b) streamlines for a spherical cell with cubic packing; (c) comparison of the trend of single cell absorption efficiency versus particle size in the two cases.

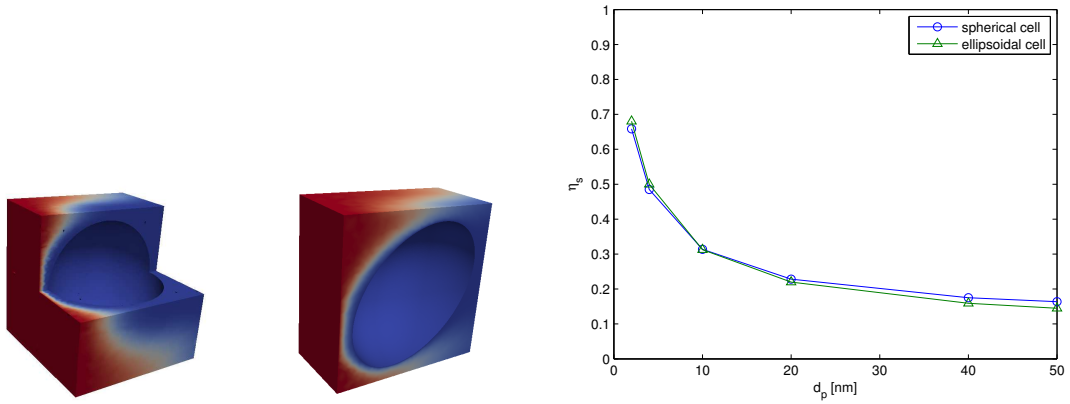

Fig. 1.9 Nanofluid motion around a single cell of different geometry at fixed porosity $\varepsilon = 0.6649$. (a) Nanoparticles concentration around a sphere; (b) nanoparticles concentration around an ellipsoid; (c) comparison of the trend of single cell absorption efficiency versus particle size in the case of different cell geometries with fixed porosity $\varepsilon = 0.6649$ and cubic packing; blue line represents spherical cell, green line ellipsoidal cell.

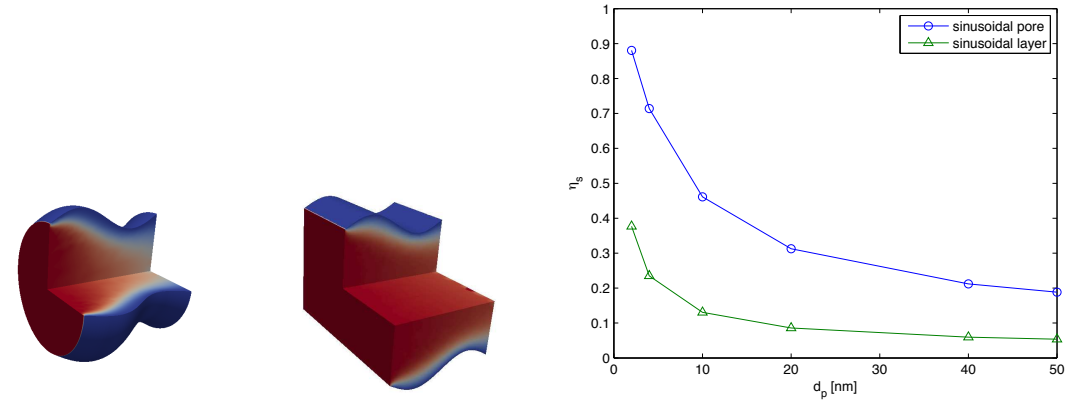

Fig. 1.10 Nanofluid motion into a pore of different geometry at fixed porosity $\varepsilon = 0.6649$. (a) Sinusoidal pore; (b) sinusoidal layer; (c) trend of single cell absorption efficiency versus particle size in the two cases; blue line represents sinusoidal pore, green line sinusoidal layer.

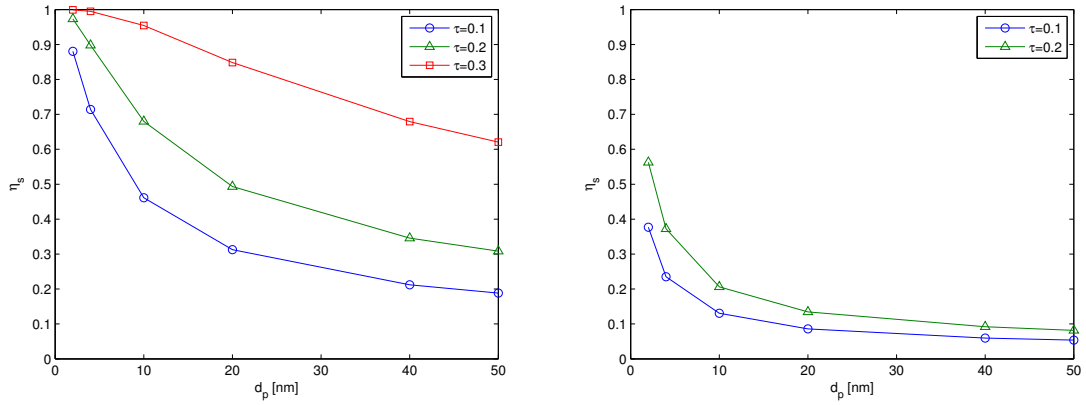

Fig. 1.11 Trend of single cell absorption efficiency versus particle size for the motion of the nanofluid into a pore with different tortuosity, in the case of (a) a sinusoidal pore, (b) a sinusoidal layer. $L = \overline{w} = 10$ μm and $\varepsilon = 0.6649$.

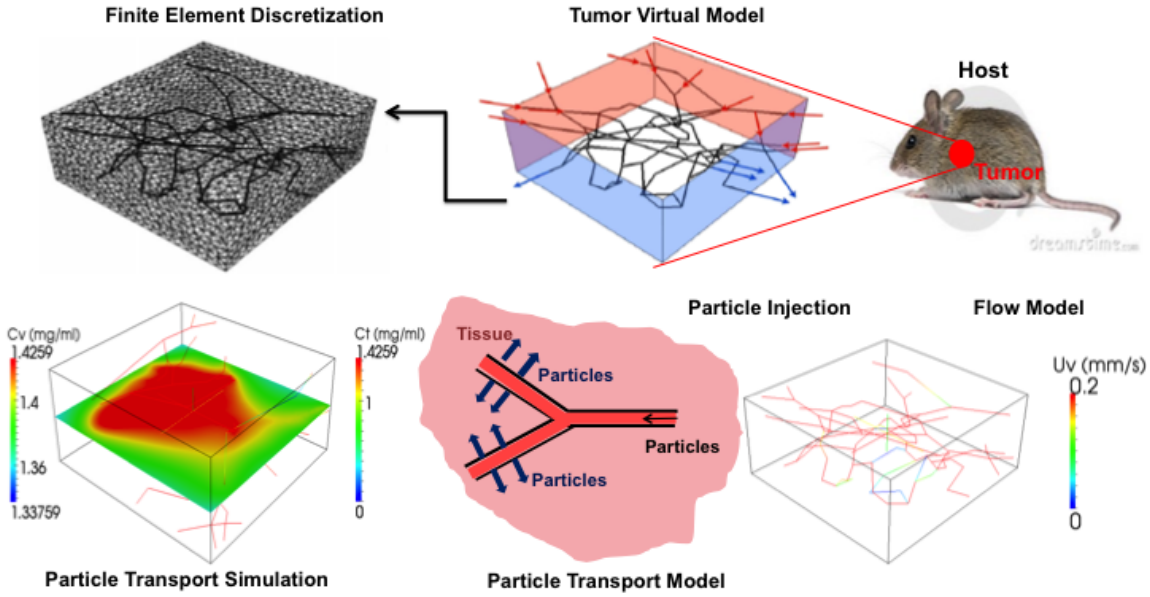

Fig. 1.12 Sketch of the VMN-based hyperthermia process, split into different phases: *i*) manufacturing of the particles; *ii*) definition of the delivery protocol; *iii*) set up of the FEM computational model; *iv*) simulation of the VMN spatio-temporal distribution; *v*) simulation of hyperthermia and study of the temperature maps.

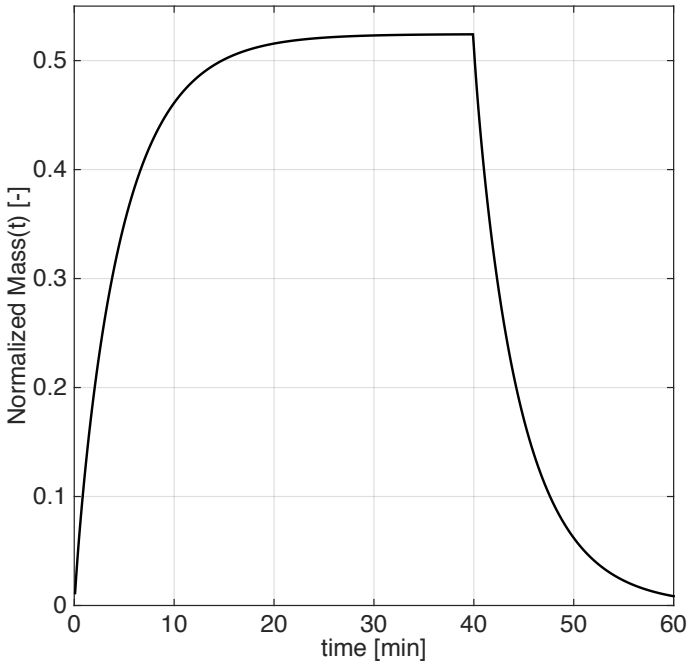

Fig. 1.13 Timecourse of particle accumulation after renormalization with respect to the amount of particles injected for 40 min.

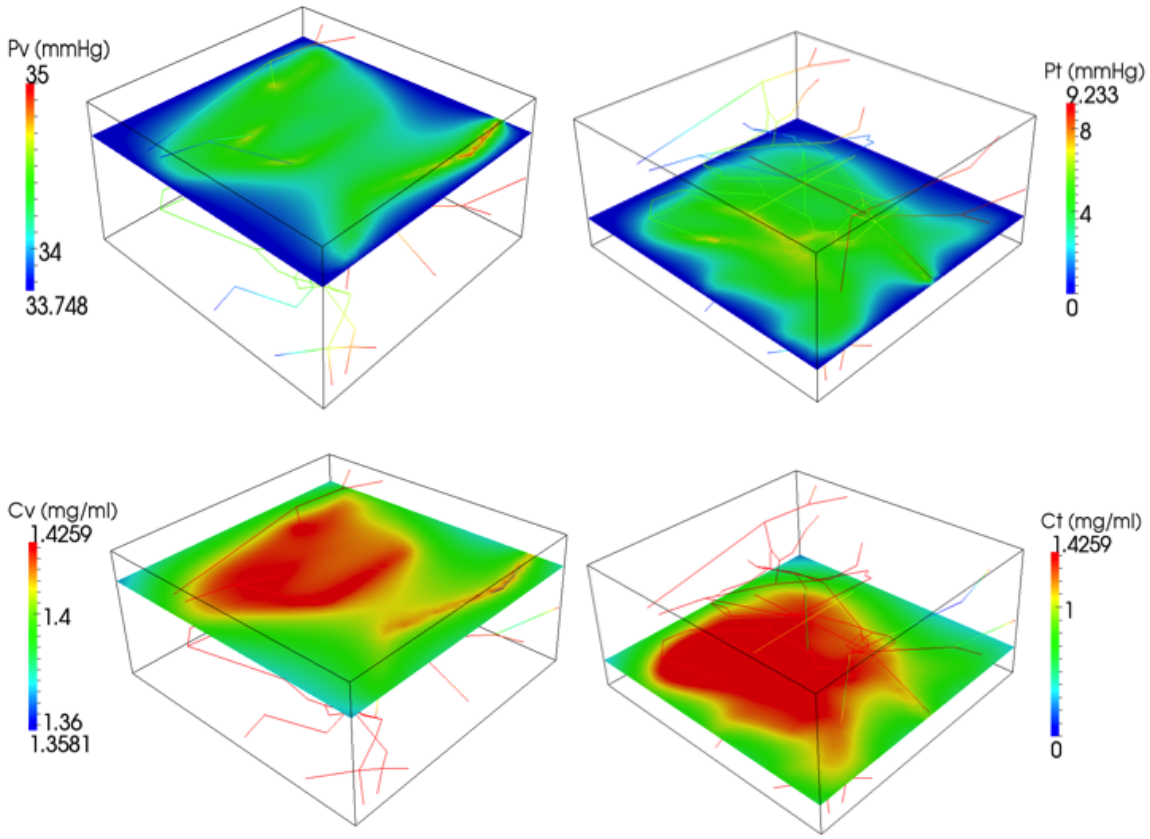

Fig. 1.14 Interstitial fluid pressure, p_t for high hydraulic permeability and absent lymphatic drainage $L_p^{LF}\frac{s}{v} = 0$ (top panel). Spatial distribution of c_t, c_v for particle delivery with constant target $c_{ref} = 1$ mg/ml (bottom panel).

Index

MOX Technical Reports, last issues

Dipartimento di Matematica
Politecnico di Milano, Via Bonardi 9 - 20133 Milano (Italy)

42/2016 Iannetti, L.; D'Urso, G.; Conoscenti, G.; Cutri, E.; Tuan, R.S.; Raimondi, M.T.; Gottardi, R.; Zu
Distributed and lumped parameter models for the characterization of high throughput bioreactors

38/2016 Quarteroni, A.; Manzoni, A.; Vergara, C.
The Cardiovascular System: Mathematical Modeling, Numerical Algorithms, Clinical Applications

39/2016 Andrà, C.; Brunetto, D.; Parolini, N.; Verani, M.
Student interactions during class activities: a mathematical model

40/2016 Miglio, E.; Parolini, N.; Penati, M.; Porcù R.
High-order variational time integrators for particle dynamics

41/2016 Giovanardi, B.; Scotti, A.; Formaggia, L.
A hybrid XFEM - Phase Field (Xfield) method for crack propagation in brittle materials

36/2016 Mancini, L.; Paganoni, A.M.
Marked Point Process models for the admissions of heart failured patients

37/2016 Tugnoli, M; Abbà, A. ; Bonaventura, L.; Restelli, M.
A locally p-adaptive approach for Large Eddy Simulation of compressible flows in a DG framework

34/2016 Menafoglio, A.; Secchi, P.
Statistical analysis of complex and spatially dependent data: a review of Object Oriented Spatial Statistics

33/2016 Antonietti, P. F.; Ferroni, A.; Mazzieri, I.; Quarteroni, A.
hp-version discontinuous Galerkin approximations of the elastodynamics equation

35/2016 Zonca, S.; Formaggia, L.; Vergara, C.
An unfitted formulation for the interaction of an incompressible fluid with a thick structure via an XFEM/DG approach